Spiess, R., Dibona, R., Rybacki, E., Wirth, R., Dresen, G. (2012): Depressurized Cavities within High-strain Shear Zones: their Role in the Segregation and Flow of SiO2-rich Melt in Feldspar-dominated Rocks. - Journal of Petrology, 53, 9, 1767-1776

DOI: 10.1093/petrology/egs032

Depressurized cavities within high strain shear zones: Their role for the segregation and flow of SiO_2-rich melt in feldspar dominated rocks

Richard Spiess*[1], Raffaella Dibona[1], Erik Rybacki[2], Richard Wirth[2] and Georg Dresen[2]

[1] Dipartimento di Geoscienze, Università di Padova, Via Gradenigo 6, 35131 – Padova - Italy.

[2] GFZ Potsdam, Telegrafenberg, D-14473 Potsdam, Germany
* corresponding author. Telephone: +39-049-8279150. Fax: +39-049-8279134. E-mail: Richard.spiess@unipd.it

ABSTRACT

We observed void growth and coalescence into cavity bearing shear bands during deformation of wet synthetic anorthite aggregates containing < 3vol% silca-enriched melt. Samples have been deformed in the Newtonian creep regime to high strain during torsion experiments at 1100 °C temperature and 400 MPa confining pressure. Localised cavity bearing shear bands show an S-C'-geometry: the bands (C') are oriented at about 30° to the compression direction of the imposed simple shear and the bands internal foliation (S) is rotated towards the horizontal external shear plane. Cavity bearing shear bands started to nucleate in the sample periphery above a shear strain threshold of ≈ 2. Quartz crystallised from the water saturated SiO_2-rich melt within large cavities inside these bands, which requires that the melt is decompressed by > 200 MPa during formation. The dynamically evolving cavities are sites of locally reduced pressure collecting the melt distributed in the adjacent matrix. Therefore, cavitation damage under ductile conditions may result in the development of an efficient melt channeling system controlling SiO_2-rich melt flow in the lower crust.

Electron Backscatter Diffraction (EBSD) analysis shows that the quartz inside the cavity bands has a crystallographic preferred orientation (CPO). The development of the CPO is explained by the preferred dissolution of crystals oriented with the rhombohedrons and trigonal dipyramids orthogonally to the compression direction and by preferential growth of crystals aligned with their <0001> axis in the extensional direction of the externally applied simple shear deformation.

Key words cavity bearing shear bands - CPO - depressurized voids - diffusion creep - melt transport

INTRODUCTION

Synthetic anorthite aggregates deformed to high strain during torsion experiments are excellent proxies to study the development of melt and fluid channelling pathways through a feldspar-dominated lower crust. Rybacki *et al.* (2008; 2010) and Kohlstedt *et al.* (2010) have performed high strain torsion experiments on anorthite aggregates in the diffusion creep regime between 950°-1200° C and 100-400 MPa confining pressures. Some of the nominally melt free aggregates used by Rybacki *et al.* (2008, 2010) carried small amounts (< 3%) of silica-enriched residual glass, whereas all aggregates except one used by Kohlstedt *et al.* (2010) contained 3 to 12% added MORB-type basaltic glass. Despite this difference, within both sets of deformed samples regularly spaced shear bands formed with an angle of about 15° to the shear plane and of 30° to the principal stress direction σ_1.

After torsion tests performed to high strains (3-5), the samples of Rybacki *et al.* (2008, 2010) exhibited abundant cavities nucleating mostly at grain triple junction and at grain boundaries. Cavitation growth has previously been observed in anorthite-diopside samples deformed in torsion by Dimanov *et al.* (2007). In those samples cavities coalesced to micro-fissures that linked to micro- and meso-cracks hundreds of micrometers in lengths. Instead, in the samples of Rybacki *et al.* (2008, 2010) at shear strains ≥ 2 an anastomozing network of regularly spaced cavity bearing shear bands formed. Because these shear bands contained the segregated residual glass phase, and because microstructural inspection suggests that growth and coalescence of the cavities is responsible for the formation of the shear bands, Rybacki *et al.*

(2008, 2010) concluded that cavitation damage in high temperature shear zones may control lower crustal melt and fluid flow.

The recently published study of Kohlstedt *et al.* (2010) is a continuation of the experimental work on deformation of melt-bearing feldspar and olivine rocks going back to Bussod & Christie (1991), Hirth & Kohlstedt (1995a,b), Kohlstedt & Zimmerman (1996), Daines & Kohlstedt (1997), Zimmerman *et al.* (1999), Holtzman *et al.* (2003a, b; 2005), and Holtzman & Kohlstedt (2007), focusing on the understanding of melt segregation and melt channelling within partially molten rocks. These authors concluded that the regularly spaced shear bands result from compaction of the partially molten rocks under an applied differential stress. Orientation of the bands is the result of two different factors: 1) preferential wetting of grain boundaries oriented at a low angle to the maximum compressive stress $\sigma 1$ (Zimmerman *et al.,* 1999; Hier-Majumder *et al.,* 2004) and 2) melt flow along a pressure gradient from bands oriented at high angles towards interconnected bands oriented at lower angles to σ_1 (Holtzman & Kohlstedt, 2007).

The experimental observations of Holtzman *et al.* (2003a, b; 2005), Holtzman & Kohlstedt (2007) and Kohlstedt & Holtzman (2009) support the hypothesis of Stevenson (1989) that spacing between melt bearing shear bands and compaction length (McKenzie, 1984) are correlated. Compaction length, δ_c, depends on permeability, k, melt viscosity, μ, bulk viscosity, λ, and shear viscosity, η, of the partially molten rock as expressed by the relation (McKenzie, 1984; Scott & Stevenson, 1986)

$\delta_c = [k[\eta + (4/3)\lambda]/\mu]^{1/2}$ (1).

The compaction length defined in eqn. (1) decreases significantly with increasing melt viscosity. Kohlstedt *et al.* (2010) have used MORB-type basaltic glass with a viscosity of 10 Pas in their anorthite torsion experiments. Hydrous leucogranitic melts are at least 2 orders of magnitude more viscous (Hess & Dingwell, 1996) and dry rhyolitic melts are several orders of magnitude more viscous (Hui & Zhang, 2007), suggesting that the compaction length of samples with a silica-enriched melt is at least an order of magnitude smaller than in MORB-containing aggregates. Because shear band spacing in the samples of Rybacki et al. (2008, 2010) is similar to that observed by Holtzman *et al.* (2003a, b; 2005), Holtzman & Kohlstedt (2007), Kohlstedt & Holtzman (2009) and Kohlstedt et al. (2010), it is possible that in the presence of a highly viscous-silica rich melt its segregation is more efficiently achieved by opening of depressurised cavities in high temperature shear zones than by differential stress driven compaction.

Here we present a detailed microstructural study of one (Pl10_1) of two anorthite aggregates from the set of samples deformed by Rybacki *et al.* (2008, 2010) containing quartz within the cavities of the shear bands. We will show that quartz crystallisation from the silica-rich melt can only occur if the cavities were strongly depressurised.

METHODS

Experimental approach

Sample material

We analysed the microfabric and microtexture of a synthetic cylindrical anorthite sample (Pl10_1), 10 mm in diameter and 6.5 mm long, containing ≈ 1 vol. % silica-rich melt. The sample belongs to a suite of samples, which were deformed experimentally in the Newtonian creep regime (Rybacki *et al.,* 2008, 2010). Starting material for sample fabrication was a fine-grained anorthite glass powder (Schott Glass-Werke) with a mean grain size of <60μm. Powder composition was nearly pure anorthite ($An_{98.8}Or_{0.2}Ab_{0.9}$ - normalised to 8O) having a trace amount of impurities such as TiO_2 (0.1%), MgO (0.007%), and Fe_2O_3 (0.01%). After cold pressing, the glass powder was hot isostatically pressed using a Paterson-type gas apparatus at 300 MPa confining pressure and at three different temperatures. The powder was initially densified above the glass transition temperature (871°C, Dresen *et al.,* 1996) for 1 hour and then further annealed for 2 hours at 1050°C, slightly above the nucleation temperature of anorthite (1024°C, *Dresen et al.,* 1996). Finally, to promote grain growth, the sample was kept for 2 hours at 1100°C.

Grains are typically prismatic with an aspect ratio of about 2.5. Assuming that the grains are rectangular with a square base, a mean grain size of 3.7 ± 0.7 μm can be calculated from the mean intercept length measured directly on SEM micrographs and the obtained stereological correction factor of 1.9 (Underwood, 1970; Dimanov *et al.,* 1998) The porosity of the sample after crystallization, determined with the Archimedes method, was ≈1% and the bulk water content was ≈ 0.17 wt %, estimated using Fourier-transformed infrared spectroscopy (FTIR) and Beer-Lambert's law with a molar extinction coefficient of 32 $L_{(H2O)}$ mol^{-1} (Beran, 1987). The calculated

values are about half as high compared to calculations using the integrated absorbance (Johnson and Rossman, 2003). Analysis of the undeformed sample shows a SiO_2-enriched residual glass content of ≈ 1 vol. % homogeneously dispersed in the sample and located at grain triple junctions.

Sample deformation

Sample Pl10_1 was deformed in torsion using a Paterson-type gas apparatus (GFZ-Potsdam) at 400 MPa confining pressure, 1100°C temperature, and a constant twist rate of ≈ 2×10^{-5} s^{-1} (corresponding to a peripheral shear strain rate of $1.6x10^{-5}$ s^{-1}), yielding a maximum shear stress of ≈ 11 MPa. The sample achieved a maximum shear strain of $\gamma = 4.2$ and underwent approximately 10% lengthening, as evaluated from the change in dimension of the sample before and after the experimental run. Before removing the stress at the end of the experiment, the sample was cooled below 600° C at a rate of 30-50° C/min, and finally the confining pressure was released.

Measured torque-twist data were converted to stress-strain data assuming power law creep. The stress-strain data indicates continuous moderate strain hardening (Rybacki *et al*., 2010). Several twist rate steppings were performed to determine the stress exponent *n* (Paterson & Olgaard, 2000; Rybacki *et al.,* 2003) revealing a value of $n \approx 1$, indicative of Newtonian creep.

Analytical techniques used for microstructural analysis

After deformation two thin sections were cut from sample Pl10_1, one parallel to the sample cylinder axis (longitudinal axial section) and one tangential to the sample surface (longitudinal tangential section). During torsion of solid cylindrical

specimens strain and strain rate increase from ~ 0 at the specimen central axis to a maximum at the sample periphery (Paterson & Olgaard, 2000). Thus in longitudinal axial sections the microstructural evolution with increasing strain and strain rate can be studied in a single sample.

For backscatter electron image analysis thin sections were chemically etched with HF vapour for 20 seconds and studied with a scanning electron microscope (CamScan Mx2500 SEM) of the Department of Geosciences (Padova). The SEM is equipped with a LaB_6 filament, the electron backscatter diffraction (EBSD) Channel 5.9 software package from HKL-technology (Oxford instruments), and a semi-quantitative EDX system for microanalysis.

For EBSD analysis the thin sections were chemically-mechanically polished (Syton-polished) to remove surface damage (Prior *et al.,* 1999) and carbon-coated with a very thin film to prevent charging without degrading the pattern quality too much. Patterns were collected manually and indexing of EBSD pattern was accepted if at least five Kikuchi bands were identified by the computer simulation and if the mean angular deviation (MAD) was lower than 1°.

RESULTS

Backscatter electron (BSE) imaging of the longitudinal axial section shows that close to the torsion axis anorthite crystals have no uniform orientation, and silica–rich melt is localised within triple junctions and occasionally also along grain boundaries (Fig. 1a). With increasing strain towards the sample periphery, anorthite crystals develop a shape-preferred orientation defining the foliation of the sample. With increasing

strain the foliation is progressively inclined towards the shear direction. At a shear strain > 2, a network of regularly spaced cavity bearing shear bands is observed. Cavities within the band are often filled with a silica-enriched melt (Fig. 1b, and crystalline quartz is observed within the bands at a shear strain > 3 (Figs. 1b and 2). Semi-quantitative EDX-analysis of the silica-rich melt reveals an SiO_2 content of 81 wt % together with Al_2O_3 and CaO contents of 12.5 and 6.5 wt % respectively.

Cavity bearing shear bands: quartz-rich and quartz-free domains

Detailed inspection of the longitudinal axial thin section using transmitted plus reflected light microscopy, EDX, and EBSD analysis reveals that quartz never appears outside the cavity bearing shear bands. Crystallization of quartz only occurs within cavity bearing shear bands at shear strains > 3 (Fig. 1b, c), occupying lens-shaped domains arranged in an en-echelon configuration that are separated from quartz-free domains (Fig. 2a).

Within these two distinct domains grain boundaries have different characteristics. Anorthite-anorthite grain boundaries in the quartz-free domains often contain melt (Fig. 1b). In contrast, within quartz-rich domains anorthite-anorthite grain boundaries are mostly closed (Figs 1b, 2b). Figure 2a shows that the orientation of the Qtz-rich domains differs from that of the cavity bearing shear bands. The bands form an angle of about 20° with the shear plane (see inset in 2b) and about 25° with the direction of the maximum principle stress, σ_1. The individual quartz-rich domains are oriented close to the shear plane. Image analysis reveals that the melt content within the

quartz-free domains inside the cavity bearing shear bands exceeds 3 %, and that the quartz content within the quartz-rich domains is close to 10 %.

Along the cavity bearing shear bands the foliation has been dragged and rotated (Fig. 2a, b). Anorthite grains inside the bands are rotated towards the main shear plane (lower right inset in Fig. 2b). The foliation is formed by the shape preferred orientation of elongate anorthite grains, whose long axes align with an angle of ≈30° to the shear plane (upper left inset Fig. 2b). Anorthite crystals forming the external foliation are frequently twinned and TEM analysis reveals that the dislocation density is very low.

The deflection of the main foliation along the cavity bearing shear bands confirms that the sense of shear along the bands is synthetic with that imposed by the torsion experiment and the bands resemble S-C' type shear bands (Fig. 2a, b). Anorthite grains of the cavity bearing shear bands have usually a lower aspect ratio (2.83±0.15) than crystals aligned parallel to the external foliation (3.11±0.12).

Quartz forms single grains with rounded to straight grain boundaries (Fig. 3). The grain size and shape appears to be controlled by the space opened between the pulled-apart anorthite grains. The average grain size of quartz is 5-6μm, but smaller (1μm) and larger (10μm) grains also exist. Occasionally, clusters of several grains occur, where very small grains with rounded grain boundaries coexist next to larger ones (Fig. 3). The large majority of quartz grains is free of internal deformation microstructures. At anorthite contacts variable intensity of quartz impingement is

evident, particularly along grain boundaries oriented orthogonally to the compression direction (Fig. 3).

Quartz textures

Analysis with EBSD reveals that quartz crystals display a weak but clearly-perceptible CPO (Fig. 4). The *c* [0001] axes preferentially align in a girdle oriented orthogonally to the compression direction and show a point maximum in the extension direction. Alignment of c-axes parallel to the compression direction is very subordinate. Poles to *a* (11-20) and *m* (10-10) prisms form weak maxima about the compression direction. One of the three positive rhombohedrons *r* (10-11) is parallel to the shear plane, whereas the other two are orthogonal. The negative rhombohedrons *z* (01-11) are dispersed in a small girdle centred on an axis oriented closely orthogonally to the shearing direction. Overall, this distribution shows that rhombohedral faces are never orthogonal to the compression direction of the external stress field. The poles to the trigonal dipyramids ε(2-1-1-2) concentrate in a shear plane parallel girdle and in a maximum orthogonal to the shear plane.

DISCUSSION

Origin of Si-enriched melt

Rybacki *et al.* (2006) showed that intracrystalline water-solubility for anorthite at the experimental conditions is about 0.04 wt%. However, the overall water content estimated for the undeformed sample Pl10 using Fourier-transformed infrared spectroscopy (FTIR) was 0.17±0.04 wt%.

The presence of a strongly silica-enriched melt in sample Pl10_1 from which quartz crystallized suggests that most of the water has been dissolved in the intercrystalline residual glass phase. It became silica-enriched during anorthite crystallisation, either because the starting An-glass was locally non- stoichiometric or/and because of a Si^{4+} substitution process within anorthite (e.g. $Si^{4+} \leftrightarrow 4H^{+}$, Rybacki et al. 2006). The solubility of H_2O in a calcium-aluminosilicate melt is about 8 wt. % at 400 MPa and 1170° C (McMillian *et al.,* 1986), and depends only slightly on composition. Assuming that sample Pl10_1 has about 1 vol. % melt and about 0.13±0.04 wt % free H_2O, dissolution of most of it in the residual glass phase would result in a water-saturated melt.

Quartz crystallisation from a water saturated melt during decompression

Understanding the crystallisation of quartz from the anorthite – quartz- H_2O system (Stewart, 1967) helps to elucidate the driving forces that have controlled the redistribution of melt from the matrix to the cavity bearing shear bands within sample Pl10_1.

Figure 5 shows that at the experimental conditions of 1100° C and 400 MPa any water saturated glass phase with a quartz content higher than 42 wt % will melt. Only melts with at least 58 wt % Qtz (composition of the eutecticum at 400 MPa) would have crystallised quartz if the system were cooled below the eutecticum temperature during deformation. Since the temperature during deformation was held constant at 1100°C, even from a water saturated pure SiO_2 melt no quartz would have crystallised, because at 400 MPa the liquidus temperature is below 1100°C.

Within the An-Qtz-H_2O system crystallisation of quartz from a water saturated melt at 1100°C and 400 MPa confining pressure requires dehydration of the melt during decompression. The exact amount of decompression is a function of melt composition, and varies from 300 MPa for a melt with a minimum quartz content of 77 wt % to > 100 MPa for an extremely quartz-rich melt (Fig. 5).

The analysed silica-rich residual melt inside the shear bands corresponds compositionally almost perfectly to a molten mixture of 34 wt % An and 66 wt % Qtz (Fig. 5). This is a differentiated melt, and we ignore the exact melt composition prior to quartz crystallization. The quantitative quartz/melt relationship inside the shear bands (Fig. 1b and c) suggests that the melt's initial Qtz content must have been significantly higher than 66 wt %. EDX analysis of melt contained within quartz-free An-aggregates deformed by Rybacki et al (2008, 2010) revealed an SiO_2 content of 90 wt % as well as Al_2O_3 and CaO contents of 6 and 4 wt % respectively, corresponding to a molten mixtures of about 17 wt % An and 83 wt % Qtz (black arrow in Fig. 5). If we take this as reference composition for the undifferentiated water saturated melt in sample Pl10_1, then >200 MPa decompression is required to crystallise Qtz from it.

Implications from quartz crystallisation for the melt segregation process

What are the implications from the above outlined quartz-crystallisation process for the understanding of the interplay between melt segregation and cavity formation?

1) The observed cavities are unlikely to result from hydro-fracturing due to melt overpressure (Rosenberg & Handy, 2000), since quartz crystallization requires significantly reduced fluid/melt pressure compared to the experimental conditions. Instead, our observations suggest that depressurised cavities form in response to grain boundary sliding (GBS), and that melt is drained by the pressure difference from the matrix into the opening cavities.

2) A certain amount of GBS is required to produce sufficiently large under-pressure for quartz crystallisation within the cavity bearing shear bands. Apparently, this under-pressure is not achieved at shear strains between 2 and 3. Cavity bearing shear bands nucleate at a shear strain >2 in the periphery. At this shear strain the relative displacement of anorthite grains is limited and only small voids open within discrete shear bands. With increasing twist the strain threshold for cavity nucleation propagate inwards and new cavities open next to the already existing bands in the more peripheral highly strained zones, resulting in larger relative displacement of anorthite crystals and bigger, more depressurized cavities. A critical shear strain >3 is necessary to depressurise the cavities to the point that quartz can crystallise from the melt sucked from the neighbouring matrix and from the smaller voids inside the cavity bearing shear bands themselves. As a consequence, quartz-rich domains arrange next to quartz-free domains inside the cavity bearing shear bands at shear strains > 3 (Fig. 2), whereas at shear strains below this critical value shear bands are quartz-free.

Two main aspects arise from the above model and need to be explained:

a) How can big depressurised cavities sustain > 200 MPa under-pressure without collapsing, when anorthite deforms at a flow stress of about 11 MPa during the experiment?

b) Why does quartz not dissolve back into the melt when the pressure in the cavities is turning back to 400MPa?

The first aspect can be explained by the rates of the processes operating inside the sample. At the experimental strain rate of $2x10^{-5}s^{-1}$, and the give stress exponent of $n \approx 1$, closure of the cavities by deformation requires orders of magnitude more time than filling them with melt, even if stress concentration around the cavities allowed anorthite to deform locally by dislocation creep. Therefore, quartz had enough time to crystallise within the large cavities.

The second aspect implies that the melt's partial water pressure inside the cavities remained at about 100 MPa, even when the pressure inside the cavities turned back to 400 MPa. Two different processes are envisaged to drive this. The pressure drop in the cavities must result in phase separation inside the melt: water exsolves to a supercritical fluid and quartz crystallizes. Differentiated melt, supercritical fluid and quartz cannot be accommodated inside the same cavities, because the volume occupied by the supercritical water expands by a factor 4 when the pressure is reduced from 400 to 100 MPa at 1100°C (Burnham *et al.*, 1969; Helgeson and Kirkham, 1974) and cannot be compensated by the higher density of quartz. The observation that quartz occupies the big cavities implies that the fluid must have migrated into empty pore space opening in the sample with progressive deformation

and associated fabric change. The amount of pore space required depends critically on the quantity of melt that decompressed and on its partial water pressure. If we hypothesise that the melt was redistributed over the full length of the shear bands, but quartz crystallized only at shear strain > 3, then maximal half of the melt in the sample dehydrated down to a partial water pressure of about 100 MPa. According to McMillan *et al.* (1986) decompression of a water saturated silica-rich melt from 400 to 100 MPa exsolves about 4.3 wt % H_2O. This arises in 0,02 wt % H_2O that must have been redistributed in the sample's open pore space, or less if the melt was water-undersaturated.

Quartz CPO

Quartz grains display a weak but clearly perceptible CPO (Fig. 4) defined by the alignment of c-axes normal to the compression direction of the applied external stress field and by the absence of rhombohedral and trapezohedral planes orthogonal to the compression direction.

Formation of a CPO during deformation is commonly associated with dislocation creep although a weak CPO in feldspar was found to develop during linear viscous creep (Gomez-Barreiro *et al.,* 2007). Activation of dislocation creep in quartz likely requires an order of magnitude higher differential stresses than those applied in our experiments (Hirth & Tullis, 1994). Therefore, we consider it unlikely that the observed CPO results from dislocation creep of quartz. Instead, the observed quartz-CPO is best explained by a mechanism implying melt assisted dissolution-

precipitation creep. This CPO formed under the control of the externally applied stress field once the quartz crystals formed a load-bearing framework inside the melt filled voids.

Tullis (1989) suggested that dissolution-precipitation creep will result in the formation of a CPO if crystallographic anisotropies control the growth- and dissolution rates of mineral surfaces. A CPO can either result from selective dissolution of crystallographic unfavourable oriented minerals within a differential stress field (Hippert, 1994), or potentially from rotation rate differences of crystals during deformation as a function of orientation and aspect ratio, the latter being controlled by the dissolution- and growth kinetics of distinct crystal surfaces (Bons & den Brok, 2000).

In our sample, dissolution of quartz is supported by impingement-microstructures (Fig. 3). Comparison of our EBSD data with crystallographic preferred orientation data of quartz deformed in the dissolution-precipitation creep regime (Becker, 1995) supports the hypothesis that the measured CPO was formed during melt assisted dissolution-precipitation creep controlled by the externally applied stress field. Becker (1995) has shown that during dissolution-precipitation creep quartz grains oriented with their c-axis at 45° to the compression direction have been dissolved by pressure solution, whereas grains oriented with their c-axis either parallel or orthogonal to the compression direction have not. He interpreted this as evidence for rhombohedrons (r {10-11}, z {01-1-1}) and trigonal dipyramides ε{2-1-12} being the

most easily dissolvable crystal faces of quartz when they are oriented orthogonally to the compression direction.

In our sample quartz rombohedrons or trigonal dipyramides are never oriented orthogonally to the compression direction of the externally applied stress field (Fig. 4). It is conceivable that crystals with these respective orientations were dissolved preferentially. In our sample c-axis are preferentially oriented in a girdle orthogonal to the compression direction with a point maximum in the extension direction. Therefore, we believe that dissolved SiO_2 has preferentially accreted crystals with these orientations.

Since the EBSD data of the quartz crystals seem just to reflect the influence of the external stress state and not of the internal stress field due to shearing of the cavity bands itself, we expect that the local strain is partitioned along the boundaries of these compact lenses.

CONCLUSIONS

The geometrical orientation and the spatial distribution of the cavity bands in our experimentally deformed anorthite aggregates are strikingly similar with those of the melt bands in the experimentally deformed samples of Holtzman *et al.* (2003a, b; 2005) and Kohlstedt *et al.* (2010). Compaction length theory cannot explain their formation, nor can the preferred wetting of grain boundaries oriented at a low angle to $\sigma 1$ (Zimmerman *et al.,* 1999; Hier-Majumder *et al.,* 2004) or the coalescence of favourably oriented melt pockets explain the formation of the cavity bands within our sample. It is likely that the slower flow rate of higher viscous silica-rich melt in our

samples inhibited the relaxation of local stress concentrations at the grain scale resulting eventually in cavity nucleation, growth and coalescence. This differences may explain the discrepancies in the formation mechanisms of melt-rich bands in the samples of Holtzman *et al.* (2003a, b; 2005), Kohlstedt *et al.* (2010) and our samples.

In our sample melt channelling bands in an S-C' geometry clearly form under Newtonian conditions at high shear strain. The melt channelling bands form in response to cavitation damage driven by cooperative grain boundary sliding not fully accommodated by diffusive mass transfer (Dimanov *et al*., 2007, Rybacki *et al.,* 2008, 2010). The cavity bearing shear bands in our sample are preferential conduits for melt transport through the deformed aggregates. There is unambiguous evidence that the opening of depressurised voids has driven melt to move from triple junctions and partially wetted grain boundaries to newly forming cavity bearing shear bands.

Our study suggests that segregation and transport of silica-rich melt is efficient in rocks undergoing cavity damage during ductile high strain deformation. Because in the crust there is a positive feedback relationship between partial melting and strain localisation (e.g. Hobbson *et al.,* 1998; Marchildon & Brown, 2001; Brown, 2004; Zavada et al., 2007; Jamieson et al., 2011), we envisage that cavitation damage within shear zones should be an important control for melt flow through the feldspar dominated ductile crust.

FUNDING

This work was supported by the Ministero dell'Istruzione dell'Università e della Ricerca [grant number PRIN 2007BWMWM8_001].

ACKNOWLEDGMENTS

We thank Ben Holtzman, David Kohlstedt and a third anonymous reviewer for their very helpful and constructive reviews.

REFERENCES

Becker A. Quartz pressure solution: influence of crystallographic orientation Journal of Structural Geology 1995;17: 1395-1405.

Beran A. OH groups in nominally anhydrous framework structures: An infrared spectroscopic investigation of Danburite and Labradorite, Physics and Chemistry of Minerals 1987;, 14: 441– 445.

Bons P J, den Brok B. Crystallographic preferred orientation development by dissolution-precipitaion creep. Journal of Structural Geology 2000; 22: 1713-1722.

Brown M. The mechanisms of melt extraction from lower continental crust of orogens, Transactions of the Royal Society of Edinbourgh: Earth Sciences 2004; 95: 35-48.

Burnham C W, Holloway J R, Davis N F. The specific volume of water in the range 1000 to 8900 bars, 20° to 900°C. American Journal of Science 1969; 267-A: 70-95.

Bussod G Y, Christie J M. Textural development and melt topology in spinel lherzolite experimentally deformed at hypersolidus conditions. Journal of Petrology 1991; Special Lherzolite Issue: 17-39.

Daines M J, Kohlstedt D L. Influence of deformation on melt topology in peridotites. Journal of Geophysical Research 1997; 102:10257-10271.

Dimanov A, Rybacki E, Wirth R, Dresen G. Creep and strain-dependent microstructures of synthetic anorthite-diopside aggregates. Journal of Structural Geology 2007; 29: 1049-1069.

Dimanov A, Dresen G, Wirth R. High-temperature creep of partially molten plagioclase aggregates. Journal of Geophysical Research 1998; 103-B5: 9651-9664.

Gómez Barreiro J, Lonardelli I, Wenk R H, Dresen G, Rybacki E, Ren Y, Tomé C N. Preferred orientation of anorthite deformed experimentally in Newtonian creep. Earth and Planetary Science Letters 2007; 264: 188-207.

Helgeson H C, Kirkham D H. Theoretical prediction of the thermodynamic behavior of aqueous electrolyte at high pressures and temperatures: I. Summery of the thermodynamic/electrostatic proprieties of the solvent. American Journal of Science 1974; 274: 1089-1198.

Hess K U, Dingwell D B. Viscosities of hydrous leucogranitic melts: A non-Arrhenian model. American Mineralogist 1996; 81: 1297-1300.

Hier-Majumder S, Leo P H, Kohlstedt D L. On grain boundary wetting during deformation. Acta Materiala 2004; 52: 3425-3433.

Hippertt J F M. Microstructures and c-axis fabrics indicative of quartz dissolution in sheared quartzites and phyllonites. Tectonophysics 1994; 229: 141-163.

Hirth G, Kohlstedt D L. Experimental constraints on the dynamics of the partially molten upper mantle 2. Deformation in the dislocation creep regime. Journal of Geophysical Research 1995a; 100: 15441-15449.

Hirth G, Kohlstedt D L. Experimental constraints on the dynamics of the partially molten upper mantle: Deformation in the diffusion creep regime. Journal of Geophysical Research 1995b; 100: 1981-2001.

Hirth G, Tullis J. The brittle-plastic transition in experimentally deformed quartz aggregates. Journal of Geophysical Research 1994; 99: 1131-11747.

Hobbson A, Bussy F, Hernandez J. Shallow-Level Migmatitization of Gabbros in a Metamorphic Contact Aureole, Fuerteventura Basal Complex, Canary Islands. Journal of Petrology 1998; 39 (5): 1025-1037.

Holtzman B K, Kohlstedt D L. Stress-driven melt segregation and strain partitioning in partially molten rocks: effects of stress and strain. Journal of Petrology 2007; 48 (12): 2379-2406.

Holtzman B K, Kohlstedt D L, Zimmerman M E, Heidelbach F, Hiraga T, Hustoft J. Melt segregation and strain partitioning: implications for seismic anisotropy and mantle flow. Science 2003a; 301: 1227-1230.

Holtzman B K, Groebner N J, Zimmerman M E, Ginsberg S B, Kohlstedt D L. Stress-driven melt segregation in partially molten rocks. Geochemistry, Geophysics, Geosystems 2003b; 4: 8607, doi:10.1029/2001GC000258.

Holtzman B K, Kohlstedt D L, Phipps Morgan J. Viscous energy dissipation and strain partitioning in partially molten rocks. Journal of Petrology 2005; 46: 2569-2592.

Hui H, Zhang Y. Toward a general viscosity equation for natural anhydrous and hydrous silicate melts, Acta Geochimica Cosmochimica 2007; 71(2): 403–416, doi:10.1016/j.gca.2006.09.003.

Jamieson R A, Unsworth M J, Harris N B W, Rosenberg C L, Schulmann K. Crustal Melting and the Flow of Mountains, Elements 2011;7: 253-260.

Johnson E A, Rossman G R. The concentration and speciation of hydrogen in feldspars using FTIR and H MAS NMR spectroscopy. American Mineralogist 2003; 88: 901-911.

Kohlstedt D L, Holtzman B K. Shearing melt out of the Earth: An experimentalist's perspective on the influence of deformation on melt extraction. Annual Review of Earth and Planetary Sciences 2009; 37: 16.1-16.33, doi:10.1146/annurev.earth.031208.100104.

Kohlstedt D L, Zimmerman M E. Rheology of partially molten mantle rocks. Annual Review of Earth and Planetary Sciences 1996; 24: 41-62.

Kohlstedt D L, Zimmerman M E, Mackwell S J. Stress-driven Melt Segregation in Partially Molten Feldspathis Rocks. Journal of Petrology 2010; 51: 9-19, doi:10.1093/petrology/egp043.

Marchildon N, Brown M. Melt Segregation in Late Syn-Tectonic anatectic Migmatites: An Example from the Onawa Contact Aureole, Maine, USA, Physics and Chemistry of the Earth (A) 2001; 26: 225-229

McKenzie D. The generation and compaction of partially molten rock. Journal of Petrology 1984; 25: 713-765.

McMillan P, Peraudeau G, Holloway J, Coutures JP. Water solubility in a calcium aluminosilicate melt. Contributions to Mineralogy and Petrology 1986; 94: 178-182.

Paterson M S, Olgaard D L. Rock deformation tests to large shear strains in torsion. Journal of Structural Geology 2000; 22: 1341-1358.

Prior D J, Boyle A P, Brenker F, *et al.*. The application of Electron Backscatter Diffraction and Orientation Contrast Imaging in the SEM to textural problems in rocks. American Mineralogist 1999; 84: 1741–1759.

Rosenberg C L, Handy M R. Syntectonic melt pathways during simple shearing of a partially molten rock analogue (Norcamphor-Benzamide). Journal of Geophysical Research 2000; 105: 3135-3149.

Rybacki E, Paterson M S, Wirth R, Dresen G. Rheology of calcite-quartz aggregates deformed to large strain in torsion. Journal of Geophysical Research 2003; 108: 1-24.

Rybacki E, Wirth R, Dresen G. Superplasticity and ductile fracture of synthetic feldspar deformed to large strain. Journal of Geophysical Research 2010, 115: B08209, doi:10.1029/2009JB007203.

Rybacki E,Wirth R, Dresen G. High-strain creep of feldspar rocks: Implications for cavitation and ductile failure in the lower crust. Geophysical Research Letters 2008;35: L04304, doi:10.1029/2007GL032478.

Rybacki E, Gottschalk M, Wirth R, Dresen G. Influence of water fugacity and activation volume on the flow properties of fine-grained anorthite aggregates. Journal of Geophysical Research 2006; 111: B3, B03203.

Scott D R, Stevenson D J. Magma solitons. Geophysical Research Letters 1984, 11: 1161-1164.

Stewart D B. Four-Phase Curve in the System $CaAl_2Si_2O_8$-SiO_2-H_2O between 1 and 10 Kilobars. Schweizerische Mineralogische und Petrographische Mitteilungen 1967; 47: 35-59.

Tullis T E. Development of preferred orientation due to anisotropic dissolution/growth rates during solution-transfer creep. EOS Transactions of the AGU 1989; 70: 457-458.

Underwood E E. Quantitative Stereology, 274 pp., Addison Wesley, Boston, Mass. 1970.

Zimmerman M E, Zhang S, Kohlstedt D L, Karat S. Melt distribution in mantle rocks deformed in shear. Geophysical Research Letters1999; 26: 1505-1508.

Zavada P, Schulmann K., Konopasek J, Ulrich S, Lexa O. Extreme ductility of feldspar aggregates–Melt-enhanced grain boundary sliding and creep failure: Rheological implications for felsic lower crust. Journal of Geophysical Research 2007;, 112: B10210, doi:10.1029/2006JB004820.

FIGURES

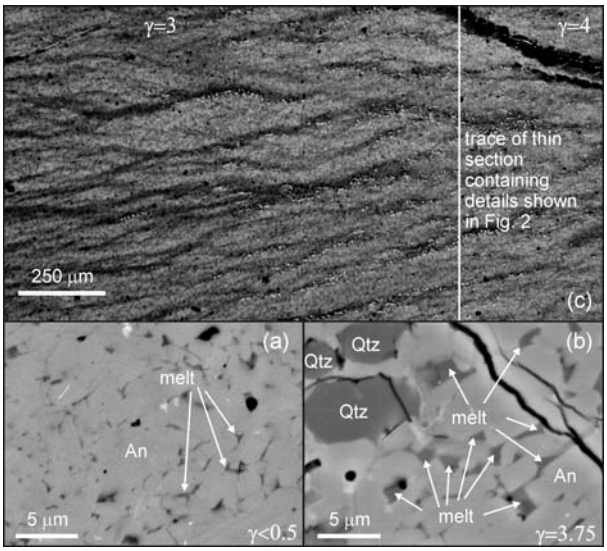

Fig. 1. (a) BSE image showing that at low shear strain close to the torsion axis ($\gamma < 0.5$) anorthite has no uniform orientation and silica-rich melt is confined mostly to triple junctions. (b) BSE image showing detail of cavity bearing shear band at high shear strain (γ 3,75). Large cavities in the upper left are quartz filled, whereas next to this quartz-rich domain smaller cavities and open grain boundaries contain silica-rich melt. (c) Reflected light image showing the distribution of cavity bearing shear bands within sample Pl10_1 cut by the longitudinal axial section. Shear strain increases from left ($\gamma \approx 2,7$) to the right ($\gamma = 4$). Bright spots inside cavity bearing shear bands are quartz-crystals, and appear for the first time at a shear strain ≈ 3.

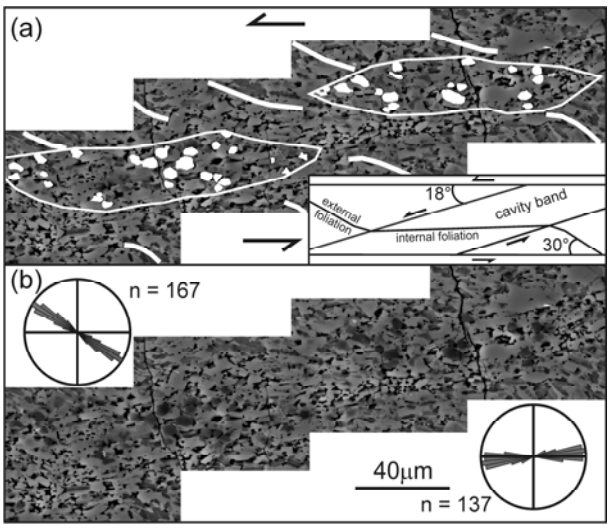

Fig. 2. Details of a cavity bearing shear band in a chemically etched longitudinal tangential section (= 3,75). (a) BSE image and sketch. Because chemical etching highlights not only compositional but also crystallographic contrasts, quartz crystals have been coloured in white. EDX and EBSD analyses were used to identify quartz. The white continuous lines trace the rotated external foliation. Quartz-rich domains are lens-shaped and exist next to quartz-free domains. Grain boundaries in the quartz-free domains are typically open. The inset shows the geometrical relationships between external foliation, internal foliation and cavity band orientation. The two horizontal lines confining the cavity bearing shear band at top and bottom in the sketch trace the orientation of the shear plane relative to that of the shear band. They do not refer to the width of the sample, which is about 150 times the width of the shear band. (b) Same BSE image as in (a) without overlays. Rose diagrams show anorthite orientation in the external foliation (upper left) and in the cavity bearing shear band (lower right).

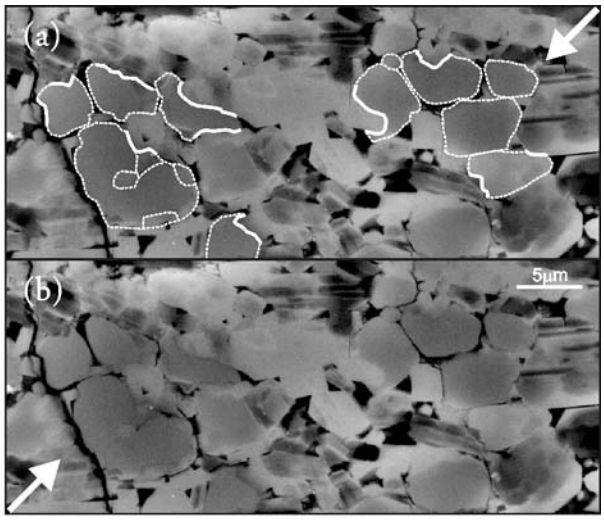

Fig. 3. BSE images of chemically etched longitudinal tangential thin section showing impingement and dissolution microstructures (thick white lines) in quartz (a). All quartz grains in the micrograph are contoured by a white hatched line. Because BSE imaging of chemically etched samples shows also crystallographic orientation contrasts (see twinned anorthite crystals), darker grey shades are not exclusive to quartz. Upper and lower edges of the microphotograph are parallel to the shear plane. Compression direction is shown by white arrows. Dissolution of quartz occurs preferentially along boundaries oriented at a high angle to the compression direction. Although quartz usually forms single grains, occasionally small grains with rounded grain boundaries coexist next to larger ones (lower left in image). (b) Same BSE image is in (a), but without contouring of quartz.

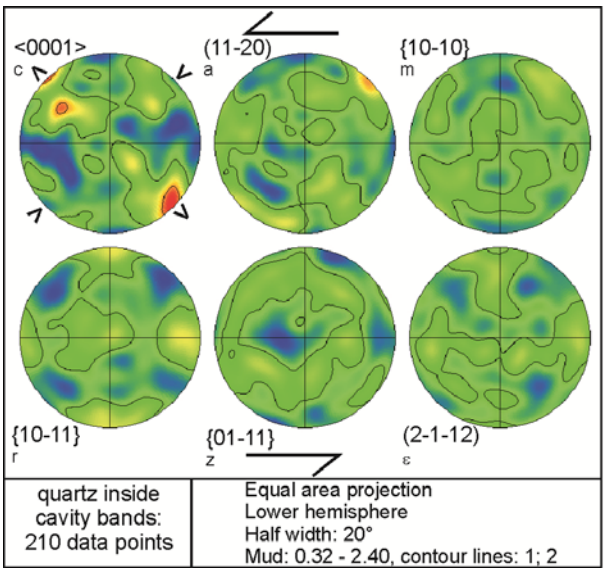

Fig. 4. Quartz crystallographic orientation data plotted in pole figures. *c*-axes plot preferentially in a girdle orthogonal to the compression direction and form a discrete maximum in the extensional direction of the external stress field. Rhombohedrons (*r*, *z*) and trigonal dipyramides (ε) are never orthogonal to the compression direction of the external stress reference frame.

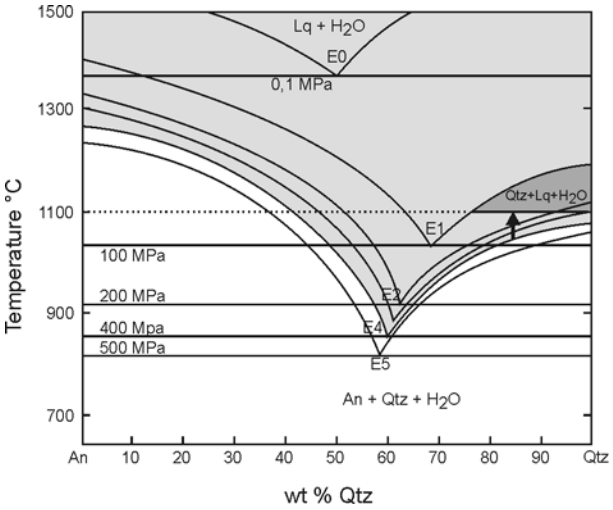

Fig 5. Projection of liquidi and solidi for water saturated melt within the An - Qtz -H_2O system at pressures between 0,1 and 500 MPa (modified from Stewart, 1967). At 1100 °C (dotted line) and 400 MPa (experimental conditions) any water saturated glass with more than 42 wt % Qtz falls in the liquidus field (light grey). Melt with more than 77 wt % Qtz can crystallize quartz, supposed the system becomes sufficiently decompressed to enter the Otz+Lq+H2O field (dark grey). The amount of decompression needed is a function of composition, and is > 200 MPa for any melt having between 77 and 90 wt % Qtz and > 100 MPa for any melt having 90 to 100 wt % Qtz. The black arrow shows minimum decompression for a melt with 83 wt% Qtz (i.e. reference melt composition). E0 to E5 are eutectica between 0,1 and 500 MPa, curved continuous lines are liquidi, and straight continuous lines are solidi between 0,1 and 500 MPa.